Ultrafast optical switching of infrared plasmon polaritons in high-mobility graphene

G. X. Ni[1,2,†], L. Wang[3,†], M. D. Goldflam[2], M. Wagner[2], Z. Fei[2], A. S. McLeod[2], M. K. Liu[2,4], F. Keilmann[5], B. Özyilmaz[1,6], A. H. Castro Neto[1], J. Hone[3], M. M. Fogler[2] and D. N. Basov[2,7]★

The success of metal-based plasmonics for manipulating light at the nanoscale has been empowered by imaginative designs and advanced nano-fabrication. However, the fundamental optical and electronic properties of elemental metals, the prevailing plasmonic media, are difficult to alter using external stimuli. This limitation is particularly restrictive in applications that require modification of the plasmonic response at sub-picosecond timescales. This handicap has prompted the search for alternative plasmonic media[1-3], with graphene emerging as one of the most capable candidates for infrared wavelengths. Here we visualize and elucidate the properties of non-equilibrium photo-induced plasmons in a high-mobility graphene monolayer[4]. We activate plasmons with femtosecond optical pulses in a specimen of graphene that otherwise lacks infrared plasmonic response at equilibrium. In combination with static nano-imaging results on plasmon propagation, our infrared pump–probe nano-spectroscopy investigation reveals new aspects of carrier relaxation in heterostructures based on high-purity graphene.

Graphene plasmonics[5-7] has progressed rapidly, propelled by the electrical tunability, high field confinement[8,9], potentially long lifetimes[10,11] of plasmons and the strong light–matter interactions[12-15] in graphene. An earlier spectroscopic study has reported photo-induced alteration of the plasmonic response of graphene on optical pumping[16]. In this work, we harnessed ultrafast optical pulses to generate mid-infrared (mid-IR) plasmons in a sample that lacks a plasmonic response at equilibrium. We examined the real-space aspects of non-equilibrium plasmon–polariton generation and propagation under femtosecond (fs) photo-excitation using a new ultrafast nano-infrared (IR) technique that fuses real-space plasmon imaging with spectroscopy. We applied this method to investigate high-quality graphene specimens encapsulated in hexagonal boron nitride: hBN/G/hBN[4].

We performed time-resolved broadband nano-IR experiments using antenna-based near-field nanoscopy (see Methods). This set-up (Fig. 1a,b) combines exceptional spatial, spectral and temporal resolution[16-18], allowing an experimental probe of the dispersion of graphene plasmons under photo-excitation—a feat previously considered technologically infeasible. In our measurements, the metalized tip of an atomic force microscope (AFM) was illuminated by a focused IR probe beam, generating strong evanescent electric fields beneath the tip. These fields possess a wide range of in-plane momenta q and therefore facilitate efficient coupling to graphene plasmons[19]. Such evanescent fields extend ~20 nm beneath the top surface of our structures, which is sufficient to

launch and detect surface plasmons in a graphene microcrystal protected by a thin (10 nm) encapsulating layer of hBN[10]. The tip of the nanoscope acts as a launcher for surface plasmons of wavelength (λ_p) that propagate radially outwards from the tip. On reflection from the sample edge, these plasmons form standing waves between the tip and the reflector. While scanning the tip towards a graphene edge, one can collect the near-field signal, which displays oscillations with a period of $\lambda_p/2$. Recent nano-IR imaging experiments with encapsulated high-mobility graphene have registered oscillations with both $\lambda_p/2$ and λ_p periodicity; the latter were assigned to plasmons launched directly from the sample edge by incident light[10].

We begin with the principal result of this work: the ultrafast dynamics of plasmons in encapsulated graphene revealed by means of nano-IR pump–probe spectroscopy (Fig. 1c,d). The broadband mid-IR probe allows for visualization of the frequency–momentum dispersion of graphene plasmons in the course of a single line-scan across the sample surface[20]. We investigated the photo-induced changes in near-field scattering amplitude $s(\omega,x)$ collected from sequential 20×20 nm^2 spatial pixels that together constitute a hyperspectral line-scan. Acquired at varying pump–probe delay times, hyperspectral scans reveal a rich spatiotemporal plasmonic response, which arises and then decays according to the dynamics of photo-excited carriers. It is instructive to present hyperspectral line-scans in the form of two-dimensional frequency-position maps $s(\omega,x)$ plotted in Fig. 1c,d (and see Supplementary Information (SI)). This representation highlights the novelty of our experimental approach, which combines non-equilibrium spectroscopy with imaging of plasmonic standing waves.

The strongest photo-induced signal is recorded at zero time delay between pump and probe pulses (Fig. 1c): we observe a set of three dispersing peaks in the $s(\omega,x)$ hyperspectral map. The dashed lines shown in Fig. 1c trace peaks of the signal determined from the spatial derivative of the raw data, $\mathrm{d}s(\omega,x)/\mathrm{d}x = 0$ (Fig. 1e). The spatial period of oscillations, as well as the relative separation between peaks and troughs, systematically increases with decreasing ω. These findings are consistent with expectations for plasmonic modes dispersing with positive group velocity.

The photo-induced plasmonic signal decays as the probe pulse is temporally delayed with respect to the pump pulse (Fig. 1d,f). After $t = 2$ ps pump–probe delay, we observe only a single peak in close proximity to the sample edge. Plasmonic features completely vanish after 5 ps (Supplementary Section 6): a timescale consistent with earlier diffraction-limited measurements[21-23]. Figure 1c,d

[1]Centre for Advanced 2D Materials and Graphene Research Centre, National University of Singapore, Singapore 117546, Singapore. [2]Department of Physics, University of California, San Diego, La Jolla, California 92093, USA. [3]Department of Mechanical Engineering, Columbia University, New York, New York 10027, USA. [4]Department of Physics, Stony Brook University, Stony Brook, New York 11794, USA. [5]Ludwig-Maximilians-Universität and Center for Nanoscience, 80539 München, Germany. [6]Department of Physics, National University of Singapore, 2 Science Drive 3, Singapore 117542, Singapore. [7]Department of Physics, Columbia University, New York, New York 10027, USA. [†]These authors contributed equally to this work. *e-mail: dbasov@physics.ucsd.edu
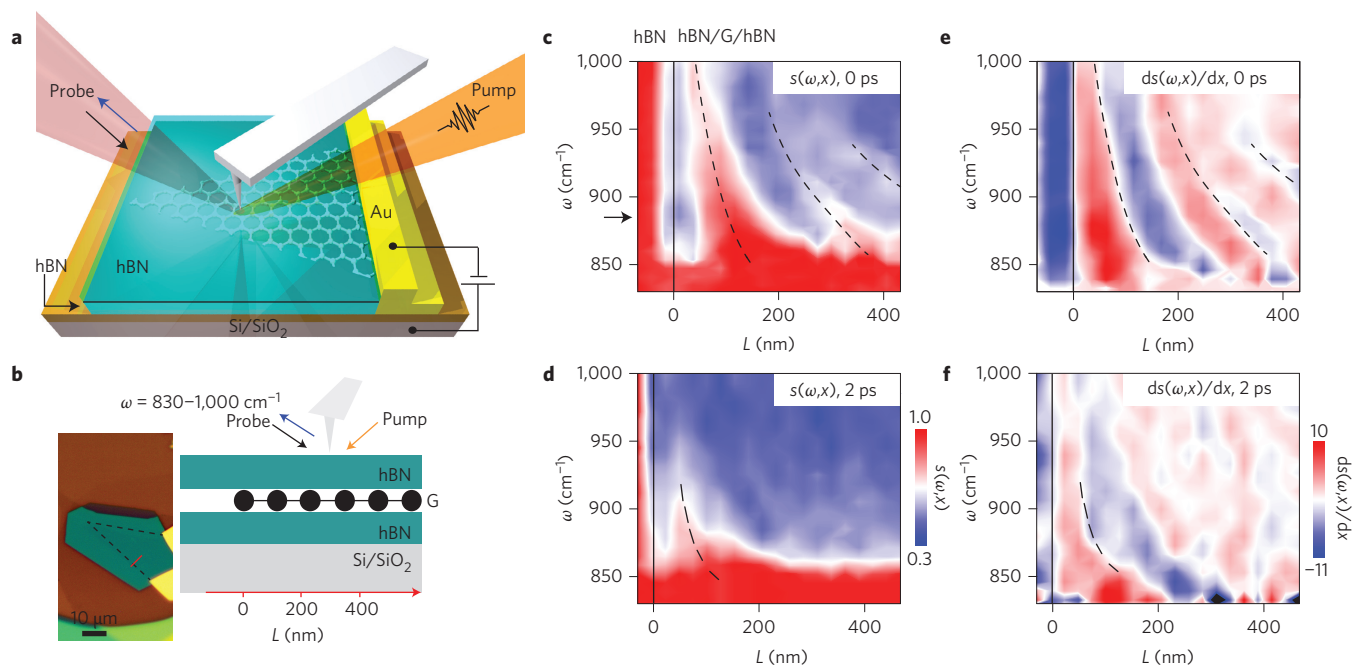
Figure 1 | Experimental configuration and ultrafast pump–probe plasmonic control. a,b, The pump–probe nano-IR set-up and optical image of the hBN/hBN device. **b**, The black dotted lines mark the graphene layer that is covered by a thin hBN layer. The red solid line denotes the nano-IR line-scan position. The probe beam spans frequencies from 830–1,000 cm^{-1}. Under pumping conditions, plasmonics polariton waves are launched by the AFM tip and reflected at the graphene edge at $L = 0$. **c,d**, Pump–probe $s(\omega,x)$ data revealing the dispersion of photo-induced plasmons for different pump–probe time delays. These data are displayed in the form of two-dimensional hyperspectral maps of the scattering amplitude $s(\omega,x)$. The black dashed lines mark the peaks of the dispersing traces obtained from $ds(\omega,x)/dx = 0$, as shown in **e,f**, and detailed in Supplementary Section 6. **e,f**, Derivatives of the pump–probe $s(\omega,x)$ data in **c,d**, respectively. The vertical solid line marks the edge of the graphene.

depicts the first direct observation of plasmon interference patterns produced by photo-excited Dirac quasiparticles.

We will now examine the physical mechanism underlying the ultrafast plasmonic effects in Fig. 1. By way of a photo-induced increase in the Drude weight (D), this transient plasmonic response originates from a strongly enhanced electronic temperature (T_{el}) in photo-excited graphene[16,23]. Specifically, at timescales longer than ~30 fs, it is expected that the optical excitation of graphene preserves the electron density, but results in an elevated T_{el} (ref. 24, for details see Supplementary Section 5). At $t = 0$, T_{el}, $D(T_{el})$, and $\lambda_p(\omega)$ are the largest. The reduction in $\lambda_p(\omega)$ shown in Fig. 1d at 2 ps following the pump pulse can be explained by a decrease of $D(T_{el})$ as electrons begin to cool. Thus, the plasmonic response observed experimentally within the first several ps following photo-excitation is consistent with the expected dynamical evolution in $D(T_{el})$.

We now proceed to survey nano-imaging data acquired for the same device using a continuous-wave (cw) laser at $\omega = 890$ cm^{-1} (Fig. 2b–d). With zero applied back-gate voltage $V_g = 0$, the near-field signal from the entire structure is nearly uniform with no optical contrast from graphene (Fig. 2b). This is because our encapsulated graphene remains nearly charge neutral even at ambient conditions ($V_g = V_{CN} = 0$ V, where V_{CN} is the charge neutrality voltage)[4]. As V_g increases, plasmon fringes start to develop, with the most prominent plasmon fringe observed closest to the sample edges. Figure 2c shows the near-field image obtained at $V_g = 60$ V. Compared with the $V_g = 0$ case, the triangular graphene shape can be clearly discerned. Moreover, multiple plasmonic fringes along the graphene edges can be detected. Increasing V_g to 115 V improves the visibility of the graphene plasmon fringes, yielding at least 12 fringes within a micrometre of the sample edge (Fig. 2d). The round-trip distance travelled by plasmons in Fig. 2 is therefore approaching 2 μm,

similar to ref. 10, and attests to a reduction of plasmonic losses in high-mobility samples.

Alternating bright and dark fringes in Fig. 2 encode information about λ_p and the dimensionless damping constant γ_p[8–11]. We recall that $\gamma_p = (\sigma_1/\sigma_2) + (\kappa_2/\kappa_1)$ is related to the ratios of the real and imaginary parts of the conductivity $\sigma(\omega) = \sigma_1(\omega) + i\sigma_2(\omega)$, and the effective permittivity $\kappa(\omega) = \kappa_1(\omega) + i\kappa_2(\omega)$ of the graphene environment[25,26] (see Supplementary Section 4). For a quantitative analysis, we plot imaging data in the form of line-profiles (Fig. 2e, f) acquired along the lines marked in Fig. 2c,d. Multiple plasmon fringes are clearly resolved in the graphene interior. These fringes appear in pairs, indicating the coexistence of two types of oscillations: one with period $\lambda_p/2$ and the other with period λ_p (Supplementary Section 3). The plasmonic line-profiles can be simulated numerically by approximating the tip as an elongated spheroid (Supplementary Section 4). The best fit, shown by the green curve in Fig. 2f, yields an estimate of $\gamma_p = 0.02$ and $\lambda_p = 150$ nm.

Our analysis of plasmonic images acquired under near-equilibrium conditions confirms the relevance of both λ_p- and $\lambda_p/2$-periodic plasmonic interference patterns to the infrared response of the high-mobility device. Nevertheless, these two distinct periodicities are not apparent in our dynamic data. This is not unexpected. Pump–probe traces show substantially broadened plasmonic fringes: an anticipated outcome of increased damping in the regime of elevated T_{el}. In Fig. 3a we display an attempt to model the influence of scattering associated with an increase in T_{el}. We start with parameters that most accurately describe our equilibrium nano-IR data (red trace), and then examine the effect of increasing γ_p. Enhanced scattering rapidly washes out weaker fringes with period $\lambda_p/2$ whereas stronger oscillations of period λ_p persist over a broader range of γ_p. Based on this analysis, we assume that separations between the dashed lines in Fig. 1c,e are equal to λ_p (Supplementary Section 3).
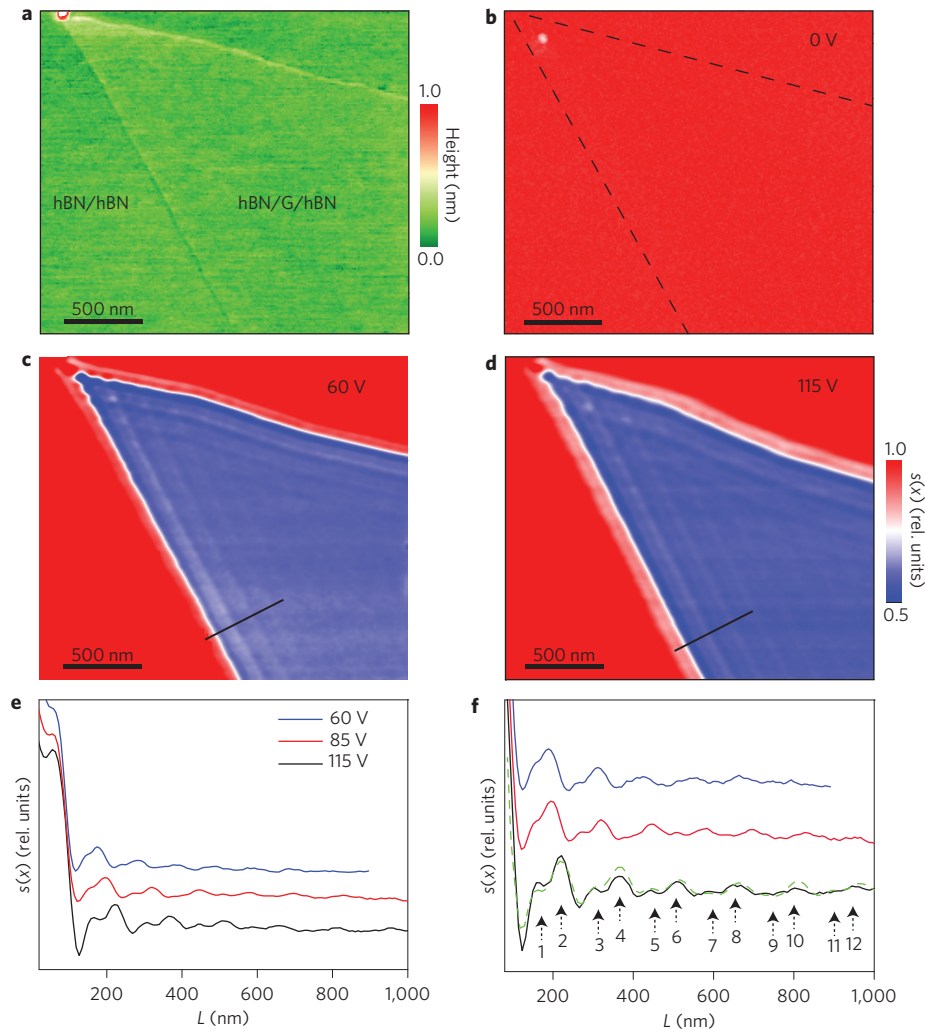
Figure 2 | AFM and static nano-IR imaging and line-profiles at different gate voltages. a, AFM topography image of the hBN/G/hBN encapsulated device. The triangular outline highlights the edges of graphene. **b–d**, Images of the normalized scattering amplitude $s(x)$ for the hBN/G/hBN structure acquired at $\omega = 890$ cm^{-1} at gate voltages of 0 (**b**), 60 (**c**) and 115 V (**d**), respectively (see Methods for details of data acquisition). In **b** the dashed lines mark the graphene position. **e,** Line-profiles across the graphene edge acquired for different gate voltages at the locations marked with black solid lines in **c** and **d**. **f**, Zoom-in of the plasmon fringes in **e**. Periodic double peaks are clearly visible. Round-trip plasmon travelling lengths of ~ 2 μm and at least 12 plasmonic oscillations are resolved in these traces. The green dashed line is the line profile obtained within a model described in Supplementary Section 3.
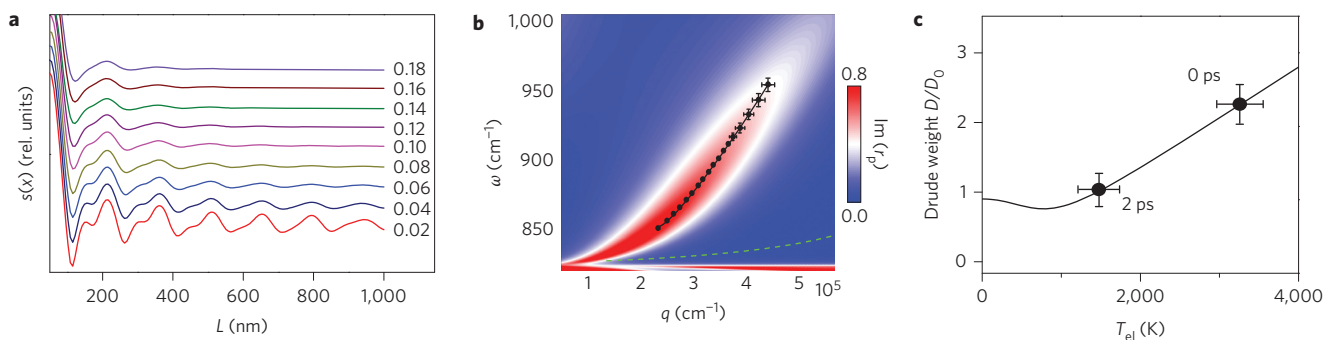
Figure 3 | Plasmonic line-profiles, dispersion and Drude weight calculations. a, Plasmon line-profiles calculated for $\lambda_p = 150$ nm at different γ_p. As γ_p increases, the fringes of period λ_p persist whereas those of period $\lambda_p/2$ diminish and become unobservable for $\gamma_p > 0.14$. **b**, The dispersion of photo-induced plasmons represented by the imaginary part of the complex reflectance Im $r_p(q,\omega)$ of our multilayered structure (Supplementary Section 5) calculated for an electron temperature of $\sim 3,200$ K at $\gamma_p = 0.15$. The black dots connected by the solid line are the experimental data obtained from Fig. 1c,e. The green dashed curve is the calculated dispersion at chemical potential $\mu = 1,330$ cm^{-1} corresponding to a gate voltage of $V_g = +30$ V. **c**, Drude weight as a function of electronic temperature calculated using equation (S3). The data point at $t = 2$ ps corresponding to $T_{el} \sim 1,700$ K was obtained from Im $r_p(q,\omega)$ calculations (Supplementary Sections 5 and 6). In both **b** and **c**, the error bars represent the 95% confidence intervals.

The dispersion of non-equilibrium photo-induced plasmons is presented in Fig. 3b. The dots were obtained from the fringe separations extracted from derivative plots in Fig. 1c,e. To model the plasmonic response we followed a standard procedure as detailed in the Supplementary Sections 2 and 5. The plasmon dispersion in Fig. 3b is visualized via a false colour map of the imaginary part of the reflectivity $r_p = r_p(q,\omega)$[16]. By varying T_{el}, we obtain a best match to the experimental data for $T_{el} = 3,200$ K. The corresponding D versus T_{el} relationship is plotted in Fig. 3c, which is similar to previous results[16]. With all parameters determined, we are at the position to plot the output of the model in the form of hyperspectral maps (Supplementary Section 5) that reproduce the gross features of the raw data in Fig. 1c. This overall agreement establishes the plasmonic origin for the real-space features observed in pump-probe data.

An important unresolved issue is the origin of the tenfold increase in the linewidth of the non-equilibrium plasmon dispersion compared with the equilibrium one. One possible candidate for the enhanced plasmon decay is the emission of acoustic phonons[10,27]. Another possibility is electron–hole scattering, for which recent relativistic hydrodynamics theories[28,29] predict that $\gamma_{ee} = (2\omega\tau)^{-1} \sim \alpha^2 T_{el}/\omega$. For $\alpha \sim 1$ and $T_{el} = 3,200$ K the estimate yields $\gamma_{ee} \sim 2.5$, which is more than an order of magnitude higher than the measured γ_p. Two possible reasons for this discrepancy are that the theory assumes undoped graphene, whereas in our case the doping is non-negligible, and the assumption of weak interactions ($\alpha \ll 1$) that may not describe the realistic case of $\alpha \sim 1$. On the other hand, the lower than expected intrinsic damping is good news for the implementation of practical ultrafast plasmonic devices using graphene.

Methods

Methods and any associated references are available in the online version of the paper.

References

1. Boltasseva, A. & Shalaev, V. M. All that glitters need not be gold. *Science* **8**, 1086–1101 (2014).
2. MacDonald, K. F., Samson, Z. L., Stockman, M. I. & Zheludev, N. I. Ultrafast active plasmonics. *Nature Photon.* **3**, 55–58 (2009).
3. Atwater, H. A. The promise of plasmonics. *Sci. Am.* **296**, 56–62 (2007).
4. Wang, L. *et al.* One-dimensional electrical contact to a two-dimensional material. *Science* **342**, 641–617 (2013).
5. Grigorenko, A. N., Polini, M. & Novoselov, K. S. Graphene plasmonics. *Nature Photon.* **6**, 749–758 (2012).
6. Basov, D. N., Fogler, M. M., Lanzara, A., Wang, F. & Zhang, Y. Colloquium: graphene spectroscopy. *Rev. Mod. Phys.* **86**, 959–993 (2014).
7. Javier García de Abajo, F. *et al.* Graphene plasmonics: challenges and opportunities. *ACS Photon.* **1**, 135–152 (2014).
8. Fei, Z. *et al.* Gate-tuning of graphene plasmons revealed by infrared nano-imaging. *Nature* **487**, 82–85 (2012).
9. Chen, J. *et al.* Optical nano-imaging of gate-tunable graphene plasmons. *Nature* **487**, 77–81 (2012).
10. Woessner, A. *et al.* Highly confined low-loss plasmons in graphene–boron nitride heterostructures. *Nature Mater.* **14**, 421–425 (2014).
11. Principi, A. *et al.* Plasmon losses due to electron–phonon scattering: the case of graphene encapsulated in hexagonal boron nitride. *Phys. Rev. B* **90**, 165408 (2014).
12. Echtermeyer, T. J. *et al.* Strong plasmonic enhancement of photovoltage in graphene. *Nature Commun.* **2**, 458 (2011).
13. Koppens, F. H. L. *et al.* Photodetectors based on graphene, other two-dimensional materials and hybrid systems. *Nature Nanotech.* **9**, 780–793 (2014).
14. Mak, K. F., Ju, L., Wang, F. & Heinz, T. F. Optical spectroscopy of graphene: from the far infrared to the ultraviolet. *Solid State Comm.* **152**, 1341–1349 (2012).
15. Brida, D. *et al.* Ultrafast collinear scattering and carrier multiplication in graphene. *Nature Commun.* **4**, 1987 (2014).
16. Wagner, M. *et al.* Ultrafast and nanoscale plasmonic phenomena in exfoliated graphene revealed by infrared pump-probe nanoscopy. *Nano Lett.* **14**, 894–900 (2014).
17. Wagner, M. *et al.* Ultrafast dynamics of surface plasmons in InAs by time-resolved infrared nanospectroscopy. *Nano Lett.* **14**, 4529–4534 (2014).
18. Eisele, L. *et al.* Ultrafast multi-terahertz nano-spectroscopy with sub-cycle temporal resolution. *Nature Photon.* **8**, 841–845 (2014).
19. Fei, Z. *et al.* Infrared nanoscopy of Dirac plasmons at the graphene-SiO$_2$ interface. *Nano Lett.* **11**, 4701–4705 (2011).
20. Dai, S. *et al.* Tunable phonon polaritons in atomically thin van der Waals crystals of boron nitride. *Science* **343**, 1125–1129 (2014).
21. Lui, C. H., Mak, K. F., Shan, J. & Heinz, T. F. Ultrafast photoluminescence from graphene. *Phys. Rev. Lett.* **105**, 127404 (2010).
22. Ulbricht, R., Hendry, E., Shan, J., Heinz, T. F. & Bonn, M. Carrier dynamics in semiconductors studied with time-resolved terahertz spectroscopy. *Rev. Mod. Phys.* **83**, 543–586 (2011).
23. Frenzel, A. J., Lui, C. H., Shin, Y. C., Kong, J. & Gedik, N. Semiconducting-to-metallic photoconductivity crossover and temperature-dependent Drude weight in graphene. *Phys. Rev. Lett.* **113**, 056602 (2014).
24. Gierz, I. *et al.* Snapshots of non-equilibrium Dirac carrier distributions in graphene. *Nature Mater.* **12**, 1119–1124 (2013).
25. Caldwell, J. D. *et al.* Sub-diffractional, volume-confined polaritons in a natural hyperbolic material: hexagonal boron nitride. *Nature Commun.* **5**, 5221 (2014).
26. Ni, G. X. *et al.* Plasmons in graphene moiré superlattices. *Nature Mater.* **14**, 1217–1222 (2015).
27. Winnerl, S. *et al.* Carrier relaxation in epitaxial graphene photoexcited near the Dirac point. *Phys. Rev. Lett.* **107**, 237401 (2011).
28. Kashuba, A. B. Conductivity of defectless graphene. *Phys. Rev. B* **78**, 085415 (2008).
29. Briskot, U. *et al.* Collision-dominated nonlinear hydrodynamics in graphene. *Phys. Rev. B* **92**, 115426 (2015).

Acknowledgements

Author contributions

All authors were involved in designing the research performing the research and writing the paper.

Additional information

Competing financial interests

F.K. is one of the cofounders of Neaspec, producer of the s-SNOM apparatus used in this study.

Methods

Devices. Our hBN/G/hBN high-quality devices were fabricated using a polymer-free multilevel stacking dry-transfer process to form the encapsulated graphene structure (Supplementary Section 1). This technique is essential for maintaining graphene flakes free of contamination, bubbles and wrinkles. Consequently, the charge neutrality point of graphene in these samples is very close to the zero gate voltage V_g at ambient conditions, as confirmed from our near-field gating experiments. After multi-stacking transfer, the metal contacts were fabricated at the exposed graphene edge[4]. Note that graphene is entirely encapsulated within the hBN flakes.

At ambient conditions, the carrier mobility near the Dirac point exceeds 140,000 cm^2 V^{-1} s^{-1}. For the carrier densities relevant to the plasmonic regime $n > 3 \times 10^{12}$ cm^{-2}, the mobility is reduced considerably. However, it still exceeds by more than an order of magnitude that of the first-generation graphene devices and approaches the room-temperature limit set by the acoustic phonon scattering[4].

Figures 1b and 2a show optical microscope and AFM images of the hBN/G/hBN device. The region of a tapered graphene microcrystal encapsulated between the two hBN layers can be clearly seen in the AFM topography. The graphene edges in our devices were preserved in their pristine state without any exposure to oxygen plasma etching, a process that is likely to introduce extrinsic edge doping and/or scattering. The underlying Si/SiO$_2$ (285 nm) substrate serves as the back gate to which we apply voltage V_g (up to 120 V at ambient conditions) to tune the carrier density in graphene[30]. Equation (S4) is based on the assumption[19] that the sheet optical conductivity $\sigma(\omega)$ of graphene is dominated by the intraband component $\sigma_{intra}(\omega) = D(T_{el})/[\pi(\Gamma - i\omega)]$.

Infrared nano-imaging experiments. The infrared nano-imaging experiments were performed using a scattering-type scanning near-field optical microscope (s-SNOM). Our s-SNOM (http://www.neaspec.com) is equipped with continuous wave mid-IR quantum cascade lasers (http://www.daylightsolutions.com) and CO$_2$ lasers (http://www.accesslaser.com). The s-SNOM is based on an AFM with a tip apex radius of 25 nm operating in a tapping frequency around 270 kHz.

A pseudo-heterodyne interferometric detection module is implemented in our s-SNOM to extract both scattering amplitude s and phase of the near-field signal. In the current work, we discuss only the former. To subtract the background signal, we demodulated the near-field signal at the third harmonic of the tapping frequency. All of the infrared nano-imaging experiments were performed under ambient conditions.

Nano-Fourier transform infrared (nano-FTIR) experiments. The ultrafast nano-FTIR set-up is based on s-SNOM. The s-SNOM is integrated with a mid-IR source (Lasnix) that emits ultrashort (<40 fs) pulses produced via an 80 MHz near-IR Er-doped fibre laser (Toptica Photonics). Pulses of mid-IR probe light are generated by difference-frequency mixing of near-IR pulses in a 2 mm thick, z-cut GaSe crystal. Ultrafast temporal resolution (~ 200 fs) is achieved by operating the s-SNOM in a pump–probe mode whereby the synchronized 40 fs near-IR pulses of the fibre laser ($\lambda = 1.56$ μm) serve as a pump with a variable pump–probe time delay.

An important technical detail of our pump–probe study is that application of 30 V back-gate voltages was necessary to achieve the plasmonic features shown in Fig. 1c,d. The static Drude weight produced by this gate voltage alone is insufficient to support steady-state plasmonic oscillations within our mid-IR probing window without photo-excitation (Fig. 3b). Previously, we carried out an analogous spatio-temporal imaging protocol on lower mobility graphene/SiO$_2$ structures[16]. Although time-resolved nano-spectroscopy revealed a pump-induced modification of the plasmonic response[16], we were unable to observe real-space plasmonic oscillations, with or without an applied gate voltage. We also wish to point out that the probe pulse in our apparatus is insufficient to launch plasmons or trigger plasmon interference patterns (Supplementary Section 6).

References

30. Das, A. *et al.* Monitoring dopants by Raman scattering in an electrochemically top-gated graphene transistor. *Nature Nanotech.* **3,** 210–215 (2008).